Check for updates

Kinetics of thermal decomposition of ammonium perchlorate with nanocrystals of Ni$_x$Co$_{1-x}$Fe$_2$O$_4$ (x = 0, 0.05, and 1) ferrites

E. A. Kammar[1] · E. A. M. Gad[2] · M. A. Mousa[1]

Abstract

Ni$_x$Co$_{1-x}$Fe$_2$O$_4$ (x = 0, 0.5, and 1) spinel nanoparticles (NPs) have been prepared using the ceramic method and Ni$_{0.5}$Co$_{0.5}$Fe$_2$O$_4$ using green, microwave, and sol–gel routes. The as-prepared materials were characterized by XRD, FT-IR, SEM TEM, and N$_2$ adsorption/desorption techniques. The catalytic activity, thermal stability, and kinetic parameters of the effect of synthesized materials upon thermal decomposition of ammonium perchlorate (AP) were studied through differential scanning calorimetry (DSC) and thermogravimetric techniques (TG). The addition of 2 mass% of nanosized ferrites to AP shifted the thermal degradation temperature of AP to lower temperatures. The catalytic activity for AP thermal degradation followed the order: NiCoF-gl > NiCoF-gr > NiCoF-mic > NiCoF-cer > NiF > CoF. The kinetic parameters for the ferrite-catalyzed reaction, using the isoconversional methods for NiCoF-gl, showed a decrease in the activation energy and preexponential factor of ammonium perchlorate thermal dissociation compared with the uncatalyzed one. The thermokinetic parameters for the catalytic decomposition process were determined and a mechanism was suggested for the kinetic reaction. The DSC results showed that the decomposition temperatures of AP decreased with the addition of the ferrites. The heat releases of the AP/ferrite mixtures were 0.82, 0.89, 0.91, 0.98, 1.04 and 1.23 kJ g^{-1} of AP, for CoF, NiF, NiCoF-cer, NiCoF-gr, NiCoF-mic, and NiCoF-gl, respectively, compared to 0.72 kJ g^{-1} for neat AP.

Keywords Ammonium perchlorate · Thermal decomposition · Kinetics of thermal decomposition · Isoconversional methods · Decomposition mechanism

Introduction

Composite solid propellants are the chief resource of chemical energy in space vehicles and missiles. Ammonium perchlorate (AP) with the chemical formulation of NH$_4$ClO$_4$ is the broadly employed energetic material and a valuable oxidizer in the composite solid propellants [1–9]. The thermal decomposition of AP is very sensitive to various additives which can usually promote the decomposition process. Comprehensive research about the thermal decomposition of AP was carried out by researchers [10]. Results indicate that

a small quantity of catalysts can reduce the thermal decomposition temperature of AP, especially that corresponding to the high-temperature decomposition (HT), increasing the apparent decomposition heat of AP, and rising the burning velocity as well as efficiency of propellant accordingly. However, till now the thermal dissociation mechanism of AP is not completely known. Therefore, many scientists have published many papers on the decomposition mechanism of AP and motivated researchers to improve new methods for speeding up the thermal decomposition and burning rate of AP. This can be done by mixing the AP with different types of compounds including metal oxides, such as CuO, NiO, Co$_3$O$_4$ [11], MgO, and Fe$_2$O$_3$ [12–15], spinel mixed-metal oxides, such as ZnAl$_2$O$_4$, MnFe$_2$O$_4$, and CuCr$_2$O$_4$ [16–18]. Compared to the single metal oxide, the complex oxides with spinel structure with a general formula of AB$_2$O$_4$, which contains two or more types of cations, showed a better catalytic activity [9, 19–21]. The A and B are di- and trivalent cations (2–3 spinels), respectively [22]. The presence of cations with different charges is at the basis of

✉ M. A. Mousa
mousa_chem@yahoo.com

E. A. M. Gad
eamgad_99@hotmail.com

1   Chemistry Department, Faculty of Science, Benha University, Benha, Egypt

2   Egyptian Petroleum Research Institute, Nasr City, Cairo 11727, Egypt

most catalytic properties of spinels, allowing internal redox reactions which make easier reduction–reoxidation cycles of the catalyst. The distribution of different cations in the tetrahedral (A) and octahedral (B) sites essentially depends on their synthetic method. The effect of this distribution on catalytic properties is not negligible. When the spinel structure is interrupted by a surface, octahedral B sites are more exposed than tetrahedral A sites. As a consequence, B sites have been considered to represent the most effective catalytic sites [23, 24]. There are marvelous studies about spinel oxides catalysts, particularly TMOs, for promoting AP thermal decomposition. For example, it was shown by Xuechun Xiao et al. that mesoporous $ZnCo_2O_4$ rods could decrease the high decomposition temperature of AP by 162.2 K [25]. Nafise Modanlou Juibari et al. demonstrated that $MnCo_2O_4$ nanoparticles prepared by the sol–gel method could reduce high decomposition temperature by 127 K [26]. Teng Chen et al. reported that $CoFe_2O_4$ NPs fabricated by solvothermal method decreased the high decomposition temperature of AP from 712.9 K to 623.4 K [27]. Ebrahim Alizadeh-Gheshlaghi et al. investigated the catalytic activity of $CuCo_2O_4$ and results showed that the high decomposition temperature of AP shifts downward about 103 K [28]. The presence of a partially filled-3d orbital in $CuCo_2O_4$ structure, so easy to accept electrons and improve the transferring electrons from perchlorate ions to the ammonium ions, which exhibits its stronger catalytic activity than probably CuO and Co_3O_4 as reported by Gheshlaghi et al. [29].

Since catalytic activity is primarily a surface phenomenon, the size reduction in the catalysts increases their catalytic activity [30]. This is because with decreasing the dimensions of the catalytic particles the surface area increases [19, 31–33]. In an oxide nanocrystal, the ratio of surface atoms to non-surface atoms is usually much larger than in a bulk material and surface species display local geometry differing from the bulk and strongly influencing chemical reactivity [34].

The catalytic efficiency of the spinel oxides also depends to a large extent on their compositions and their morphological structure, particle size, and surface properties which can be affected by the synthetic methods. The spinel oxides nanoparticles can be synthesized by numerous synthetic methods including hydrothermal [35] precipitation [36] sol–gel [37], and microemulsion [37].

The purpose of our present work is to fabricate nanostructures of $Ni_xCo_{1-x}Fe_2O_4$ (x = 0, 0.5, and 1) through different methods (ceramic, green, microwave, and sol–gel) to investigate and compare the catalytic activity of the prepared mixed metal oxides on the thermal decomposition of ammonium perchlorate. The characterizations of the synthesized samples were researched by FT-IR, XRD, SEM, TEM, and BET techniques. The DSC and TG techniques were used for studying the burning rate and the kinetics of thermal degradation of a neat AP and catalyzed AP with $Ni_xCo_{1-x}Fe_2O_4$ (x = 0, 0.5, and 1) spinel nanoparticle. The suitable reaction mechanism and the thermodynamic parameters of the catalyzed reaction are reported.

Materials and methods

Cobalt nitrate $(Co(NO_3)_2 \cdot 6H_2O)$, nickel nitrate $(Ni(NO_3)_2 \cdot 6H_2O$, ferric nitrate $Fe(NO_3)_3 \cdot 9H_2O$, and NaOH were obtained from Merck. Ammonium perchlorate (AP) of 99.8% purity was supplied from Aldrich and employed as received. Gelatin type B was provided from Sigma-Aldrich and Hibiscus flower/leaves from the local market. Deionized water was used in all the experimental methods.

Preparation of hibiscus flower extract

The extract was made by boiling 25 g of dried flowers in 200 mL deionized water for 1 h, then cooling to room temperature before filtering. The extract contains many chemical constituents, such as phenols, reducing sugars, alpha-hydroxy acids, and amino acids [38].

Preparation of ferrites

Ceramic method

Mixtures of the metal nitrates in an appropriate molar ratio (2.91 g nickel nitrate and 8.08 g ferric nitrate to form $NiFe_2O_4$; 2.91 g cobalt nitrate and 8.03 g ferric nitrate to form $CoFe_2O_4$, 2.455 g nickel nitrate, and 2.455 g cobalt nitrate and 8.03 g ferric nitrate to form $Ni_{0.5}Co_{0.5}Fe_2O_4$) were mixed with NaOH and NaCl in the ratio of 1:8:10 and pulverized together in an agate mortar for 1 h. The blends were then calcined at 1023 K for 2 h. The powders were crushed and well washed with deionized water and dried at 368 K for 1 h and heated up to 973 K with a heating rate of 5 K min^{-1}. The samples were denoted as CoFe, NiFe, and NiCoFe-cer.

Green–hydrothermal method

2×10^{-3} mol of $Fe(NO_3)_3 \cdot 9H_2O$, 5×10^{-3} mol of $Co(NO_3)_2 \cdot 6H_2O$, 5×10^{-3} mol $Ni(NO_3)0.6H_2O$, and 0.1 g of gelatin were dissolved together in 200 mL of deionized water under stirring for 1 h. This is followed by adding one molar NaOH dropwise until a pH of 10. The acquired solution was put in a Teflon-lined stainless autoclave and heated in an oven at 473 K for 6 h, and then left to be cooled naturally to room temperature. The acquired precipitate was gathered and washed five times with deionized water and lastly dried

at 373 K in an oven for 24 h [39]. The sample is denoted as NiCoFe-gr.

Microwave method

Ni$_{0.5}$Co$_{0.5}$Fe was also prepared by the microwave technique, where a mixture of 2×10^{-2} mol of Fe(NO$_3$)$_3$·9H$_2$O, 5×10^{-3} mol of Co(NO$_3$)$_2$·6H$_2$O, 5×10^{-3} mol Ni(NO$_3$)0.6H$_2$O were dissolved in 100 mL deionized water. This is followed by adding one molar NaOH solution slowly into the solution until a pH of 10 under microwave irradiation; microwave power is 600 W, irradiation time 25 min (40 s On, 40 s Off). The suspended solution obtained was allowed to cool at room temperature for 30 min, followed by centrifuging for 15 min at 3000 rpm, then washing with deionized water and alcohol five times. The obtained precipitate was allowed to dry in an oven at 373 K for 5 h. Finally, the precipitate was calcined at 1023 K for 4 h [40]. The sample is denoted as NiCoF-mic.

Sol–gel method

A mixed powder of 2×10^{-2} mol of Fe(NO$_3$)$_3$·9H$_2$O, 5×10^{-3} mol of Co(NO$_3$)$_2$·6H$_2$O, 5×10^{-3} mol Ni(NO$_3$)·6H$_2$O and 0.1 g gelatin were dissolved together in 175 mL of deionized water under stirring at 323 K for 2 h. The solution was then heated up to ~ 353 K with stirring to make a gel, which was calcined at 623 K for 2 h with a heating rate of 10 K min^{-1} to remove the remaining organic matter. Finally, the obtained powder was calcined for 7 h at 1023 K using a heating rate of 10 K min^{-1} [41]. The sample is denoted as NiCoFe-gl.

Characterizations

The phases and crystal structures of the as-prepared materials were investigated by XRD using the Shimadzu model: XRD 6000 employing CuKα ($\lambda = 0.154$ nm) radiation, with a diffraction angle between 20º and 80º. The FTIR spectrum of the NiFe$_2$O$_4$ nanoparticles was taken using an FTIR model Bruker IFS 66 W Spectrometer. The morphology of the nanoparticles was examined by the SEM and TEM techniques using Hitachi (HHS-2R) and Philips CM10 instruments, respectively. A NOVA2200e gas sorption analyzer (Quantachrome Corp.) was employed to record nitrogen adsorption/desorption isotherms for specific surface areas and porosity assessment.

Catalytic activity test

The performance of the prepared ferrites as a catalyst for the thermal degradation of ammonium perchlorate was studied using the TG and DSC techniques. AP and the spinel were initially mixed at a mass ratio of 2:98 in acetone and stirred for 30 min. followed by filtration and drying in a desiccator. The thermal analysis was performed using, respectively, a thermogravimetric analysis TGA (Perkin–Elmer TGA Q500 V20.13) at different heating rates of 5, 10, 15, and K min^{-1} from 303 to 873 K, and a differential scanning calorimetry (Perkin–Elmer DSC8000) at a heating rate of 10 K min^{-1} from 373 to 773 K. To diminish the exothermic self-heating, the thermal analyses were done on small (1–2 mg) samples.

Theoretical approach

The thermal decomposition kinetics of the studied materials were investigated using the following commonly rate equation [42]

$$\frac{d\alpha}{dt} = k(T)f(\alpha) \tag{1}$$

where k is the rate constant of the decomposition process and $f(\alpha)$ is a conversion factor in which α is:

$$\alpha = \frac{(X_0 - X_t)}{(X_o - X_f)} \tag{2}$$

where X_t, X_o, and X_f are the masses of the sample at time t, starting, and final decomposition process, respectively. The integration of Eq. (1) is:

$$g(\alpha) = kt \tag{3}$$

and k depends on temperature according to Arrhenius Eq. (4)

$$k = Ae^{-\frac{E}{RT}} \tag{4}$$

where A is the frequency factor, E is the apparent activation energy, R is the gas constant and T is the absolute temperature. By combining Eqs. (1) and (4), the next equation is obtained:

$$\frac{d\alpha}{dt} = Ae^{-\frac{E}{RT}}f(\alpha) \tag{5}$$

For a dynamic TGA process, the heating rate, $\beta = \frac{dT}{dt}$ can be introduced into Eq. (5) to give the following equation:

$$\frac{d\alpha}{dT} = \frac{A}{\beta}e^{-\frac{E}{RT}}f(\alpha) \tag{6}$$

The $f(\alpha)$-function depends on the reaction mechanism and can commonly be written as:

$$\int_0^\alpha \frac{d\alpha}{\alpha^j(1-\alpha)^q[-\ln(1-\alpha)]^p} = g(a) = \frac{A}{\beta}\int_0^T \exp\left(-\frac{E_a}{RT}\right)dT \tag{7}$$

where j, q, and p are exponent factors, one of them always being zero [42, 43]. The solutions of the left-hand side of

Eq. (7) depend on the definite representation of the function $f(\alpha)$ and are symbolized as $g(\alpha)$, which depends on the conversion mechanism and its mathematical model [43–46]. The most common reaction mechanisms operating in solid-state reactions using $f(\alpha)$ or $g(\alpha)$ are given in Supplementary Table 1 [46, 47].

There are two different mathematical methods to calculate kinetic parameters for the thermal decomposition of AP samples. The first one is model-free methods (iso-conversional technique), while the second method is known as model-based methods (model-fitting methods) as it depends upon the different reaction models given in Suppl. Table 1.

The model-free methods are based on evaluating the Arrhenius parameters without relying upon the reaction mechanism [48]. The model-free method is also called isoconversional, as the reaction rate is a function of the temperature at a constant extent of conversion [49]. To use these methods, a series of experiments were performed at different heating rates. In the present work, the Kissinger [50], Ozawa–Flynn–Wall (OFW) [51], Kissinger–Akahira–Sunose (KAS) [52], Starink [53], and Friedman [54], listed in Table 1, are used which show the most popular representatives of the isoconversional approach.

$T_{\alpha,i}$ is the temperature at which the extent of conversion α is reached under ith heating rate, T_p is the dissociation temperature peak, E_a is the apparent activation energy at the extent of conversion α, and R is the universal gas constant.

To increase the accuracy of the kinetic parameters calculated by the model-free methods an iterative procedure was used according to the following equations:

$$\ln \frac{\beta}{H(x)} = \ln\left(\frac{AE}{g(\alpha)R}\right) - 5.3305 - 1.5016\frac{E_a}{RT} \qquad (8)$$

$$\ln \frac{\beta}{h(x)T^2} = \ln \frac{AR}{g(\alpha)E} - \frac{E_a}{RT} \qquad (9)$$

$h(x)$ is expressed by the fourth Senum and Yang approximation formula [55]

$$h(x) = \frac{x^4 + 18x^3 + 86x^2 + 96x}{x^4 + 20x^3 + 120x^2 + 240x + 120} \qquad (10)$$

where $x = \frac{E_a}{RT}$ and $H(x)$ is equal to [56]

$$H(x) = \frac{h(x)x^{-2}\exp(-x)}{0.0048\exp(-1.0516x)} \qquad (11)$$

The detailed iterative procedure used to perform the activation energy computation is given elsewhere [57].

The second approach for calculating the kinetic parameters, which is known as model-fitting methods, assumes that a particular reaction model represents the conversion dependence of the reaction rate [58]. The most commonly

Table 1 The most common calculation methods used in the present work

Method	Expression	Plots	Ref
Kissinger	$\ln\left(\frac{\beta_i}{T_p^2}\right) = \ln\left(\frac{AR}{E_a}\right) + \frac{1}{T_p}\left(\frac{-E_a}{R}\right)$	$\ln\left(\frac{\beta_i}{T_p^2}\right)$ vs. $\frac{1}{T_p}$	[50]
Ozawa–Flynn–Wall (OFW)	$\ln\beta = \ln\left(\frac{AE}{g(\alpha)R}\right) - 5.3305 - 1.5016\frac{E_a}{RT_\alpha}$ $\ln\beta = \ln\frac{AE}{R} - 5.331 - 1.5016\frac{E}{RT_p}$	$\ln\beta$ vs. $\frac{1}{T_\alpha}$ or used T_p	[51]
Kissinger–Akahira–Sunose (KAS)	$\ln\frac{\beta_i}{T_{i,\alpha}^2} = \ln\frac{AE}{g(\alpha)R} - \frac{E_a}{RT}$	$\ln\frac{\beta_i}{T_{i,\alpha}^2}$ vs. $\frac{1}{T_\alpha}$	[52]
Starink	$\ln\frac{\beta}{T^{1.92}} = \ln\left(\frac{AR^{0.92}}{g(\alpha)E_a^{0.92}}\right) - 0.312 - 1.008\frac{E_a}{RT}$	$\frac{\beta}{T^{1.92}}$ vs. $\frac{1}{T}$	[53]
Friedman	$\ln\left(\frac{d\alpha}{dt}\right) = \ln[Af(\alpha)] - \frac{E_a}{RT}$	$\ln\left(\frac{d\alpha}{dt}\right)$ vs. $\frac{1}{T}$	[54]

used model-fitting method is Coats–Redfern (CR) approximation, described by Eq. (12) [59]

$$\ln\left(\frac{g(\alpha)}{T^2}\right) = \ln AR\left(\frac{\beta}{E_a}\right) - \frac{E_a}{RT} \tag{12}$$

This equation was applied to the different reaction models listed in Suppl. Table 1, and the best-suited model for fitting was defined as the solid-state reaction mechanism.

Results and discussion

XRD analysis

The XRD patterns of the investigated materials, Fig. 1, demonstrate the characteristic peaks of ferrites with the most intense peak (311), which approves the creation of a cubic spinel structure, with the (JCPDS 22-1086) for $CoFe_2O_4$ and (JCPDS 10-0325) for $NiFe_2O_4$. The peaks at values corresponding to $2\theta \sim 30.5°$, $36.1°$, $37.3°$, $43.5°$, $53.5°$, $57.1°$, and $63.5°$ are indexed to (220), (311), (222), (400), (422), (511) and (440) crystal planes, respectively. The crystallinity degree (N_c) of the ferrite samples is evaluated by comparing the integrated intensity of the 311-peak of each ferrite with that of the CoF sample [60]. The results obtained
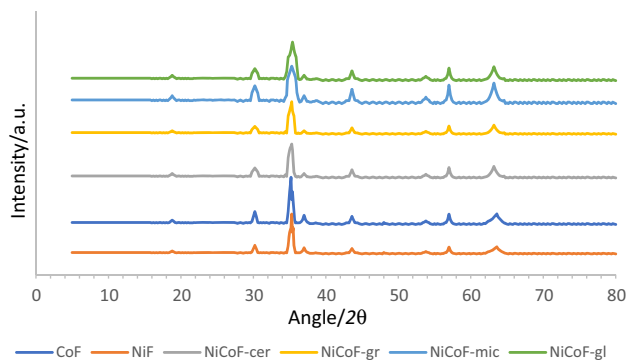
are given in Table 2. The positive value of N_c refers to the enhancement in the crystallinity compared with the CoF and the negative value indicates the decrease in crystallinity. Table 2 shows that the crystallinity increases in the order: NiF > CoF > NiCoF-cer > NiCoF-gr > NiCoF-mic > NiCoF-gl.

The crystallite sizes (D_{XRD}) of the samples were estimated by Scherrer's equation [61]:

$$D_{XRD} = 0.9\lambda/\beta^/ \cos\theta \tag{13}$$

where λ is the wavelength of the radiation, $\beta^/$ is the peak width at half the maximum intensity of the peak (311). The calculations showed that all ferrite samples were produced in nanocrystallite sizes between 19 and 46 nm, Table 2.

FTIR studies

FT-IR spectra of the investigated materials are shown in Fig. 2 and Suppl. Figure 1 and summarized in Table 2. The vibration bands (v_1) (564–600 cm^{-1}) and (v_2) (465–495 cm^{-1}) are ascribed to the stretching vibrations of tetrahedral and octahedral sites of inverse spinel ferrites, respectively [62–64]. The variation in the band locations of the different samples is attributed to the change in the distance of Fe^{3+}–O^{2-} in the equivalent crystal net sites [65]. The existence of a long shoulder at the band of the
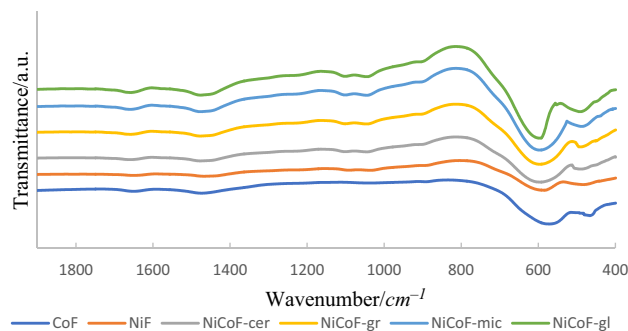

Fig. 1 XRD of the investigated ferrites

Fig. 2 FT-IR of the investigated ferrites

Table 2 Crystallinity FT-IR, cationic mass percentages, particle size, and surface area data of the investigated samples

Sample	XRD particle size/nm	TEM particle size/nm	Crystallinity	ν_1/cm^{-1}	ν_2/cm^{-1}	BET-surface area/cm^{2}g^{-1}	Pore radius/nm	Ni Mass%	Co	Fe
CoF	41	39	–	571	465	54	3.1	–	25.01	47.70
NiF	46	44	0.1332	584	484	62	3.5	25.07	–	47.62
NiCoF-cer	34	33	0.1212	593	487	68.2	4.4	12.50	12.48	47.55
NiCoF-gr	29	26	− 0.0132	595	490	73.1	5.3	12.51	12.47	47.57
NiCoF-mic	24	21	− 0.0223	593	486	88.7	6.5	12.50	12.49	47.54
NiCoF-gl	19	17	− 0.0456	596	491	99.6	8.0	12.51	12.47	47.56

Fig. 3 SEM images of **a** NiF, **b** CoF, **c** NiCoF-cer, **d** NiCoF-gr, **e** NiCoF-mic, and **f** NiCoF-gl
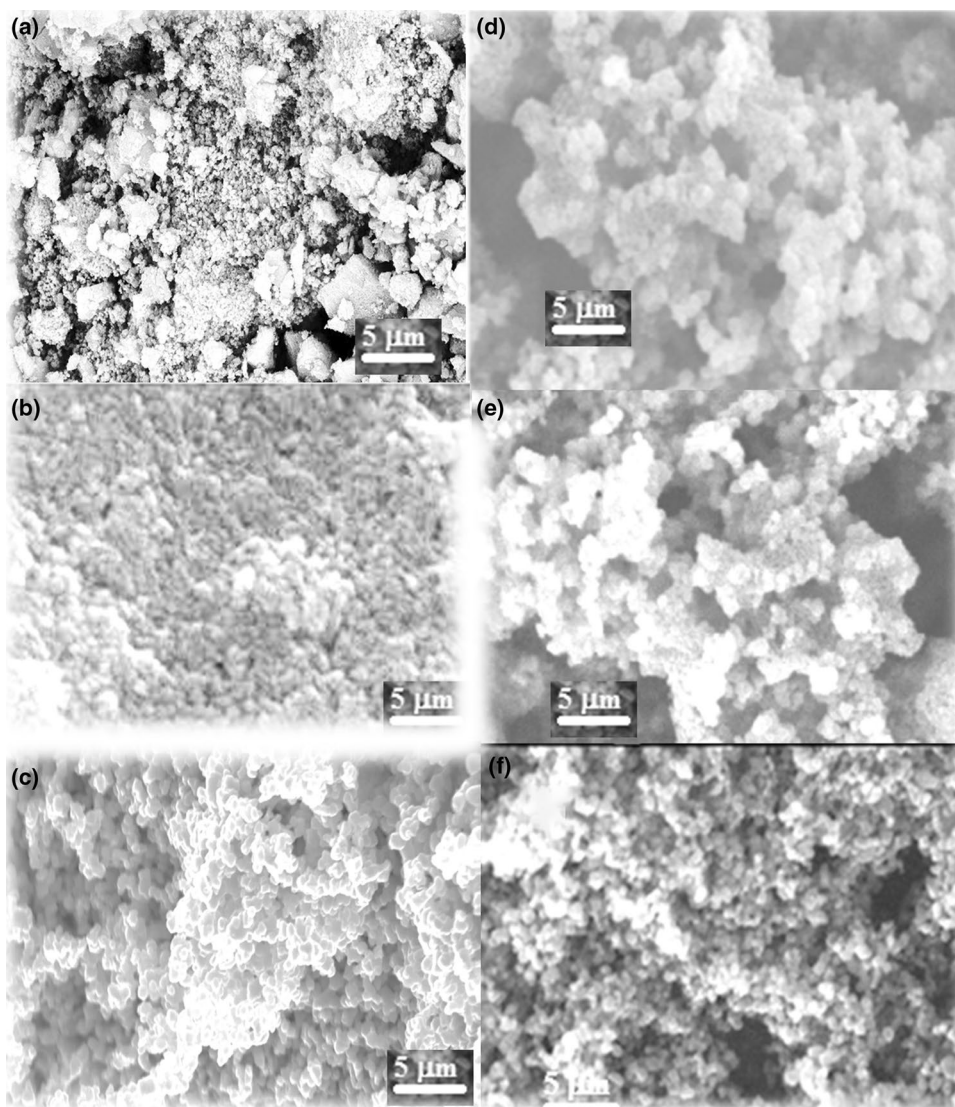
tetrahedral site is indicative of the presence of other ionic states in that site [66].

SEM and TEM

The surface structure and morphology of the investigated spinel samples were analyzed using the SEM and TEM images shown in Figs. 3 and 4. The SEM micrographs of the samples, Fig. 3, show different structures with heterogeneous surfaces depending on the preparation method. The TEM images, Fig. 4, illustrate deformed spherical particle shapes with particle sizes that agree to some extent with those found by XRD, Table 2. The elemental compositions of the ferrites were analyzed by the X-ray fluorescence (XRF) method and the mass percentage of Ni, Co, and Fe matched well with the proposed ferrite compositions, Table 2.

Surface textural properties

The N_2 adsorption–desorption isotherm of the investigated samples is represented in Fig. 5, which shows a mesoporous structure with an isotherm of type IV and V according to the IUPAC classifications. The hysteresis loop observed at the higher relative pressure (p/p^o) for the ferrite sample refers to its macropore structure. The hysteresis loops of the samples prepared by ceramic methods are H3 type referring to non-rigid aggregates of plate-like particles (slit-shaped pores), whereas the other samples exhibit H1 type corresponding to favorably cylindrical pore channels. The BET-surface area and pore size diameter acquired from the analysis of nitrogen adsorption–desorption isotherm data are given in Table 2, which demonstrates that both the surface area and pore size increase with reducing the particle size according to the following order:
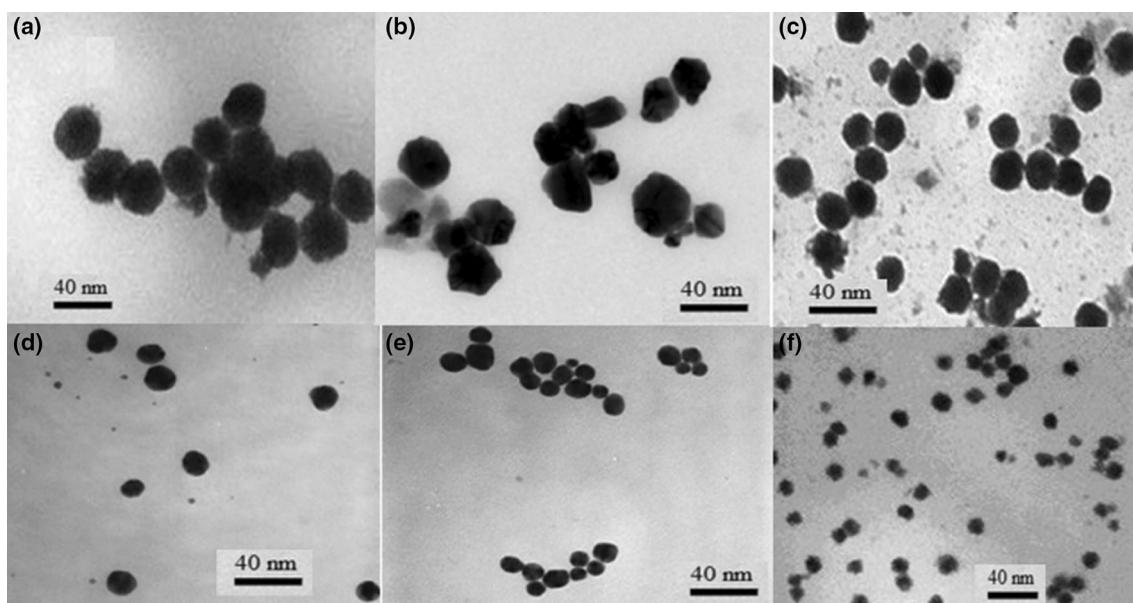
Fig. 4 TEM images of **a** NiF, **b** CoF, **c** NiCoF-cer, **d** NiCoF-gr, **e** NiCoF-mic, and **f** NiCoF-gl

NiCoF-gl > NiCoF-mic > NiCoF-gr > NiCoF-cer > NiF > CoF.

Catalytic study

The catalytic activity of the investigated ferrites toward the thermal decomposition of ammonium perchlorate (AP) was investigated with differential scanning calorimetry (DSC). The results indicated that the small quantity of the ferrite catalysts can reduce the thermal decomposition temperature of AP, especially that corresponding to the high-temperature decomposition (HT), improving the apparent decomposition heat of AP, and increasing the burning velocity and efficiency of propellant accordingly. The DSC-curves of AP decomposition in the absence and presence of 2% mass of
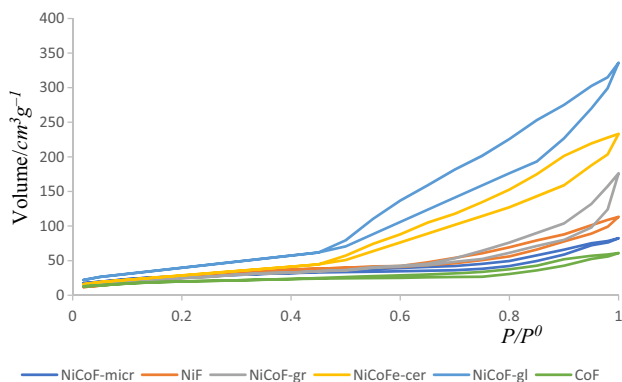

Fig. 5 BET plots of the investigated ferrites

ferrites at the heating rate of 10 K min^{-1} are given in Fig. 6. The curve for neat AP has an endothermic temperature of about 518.1 K, which is ascribed to the transition from the orthorhombic to the cubic phase, and two exotherms with peak maximum temperatures of 610.1 and 742.2 K, respectively [67]. The first exothermic peak at low temperature (LT) is attributed to the partial decomposition of AP. The second or high-temperature exothermic peak (HT) corresponded to the complete decomposition of the intermediate product into a volatile product [67].

Compared with the pure AP, Fig. 6 shows a clear difference for AP decomposition in the presence of the ferrites. All curves show an endothermic peak at more or less the same temperature obtained for pure AP indicating that the crystallographic phase transition hasn't been affected by the additive of the ferrites, while both the LT- and HT-peaks are significantly shifted to lower temperatures (Fig. 6b–e) indicating that the ferrites can lower the thermal decomposition of AP. The specific thermal decomposition temperature data are summarized in Table 3. The HT peaks of AP containing the 2% as catalysts are 730.3, 724.2, 692.1, 671.2, 641.3, and 623.1 K, for CoF, NiF, NiCo-cer, NiCoF-gr, NiCoF-mic, and NiCoF-gl, respectively. The results indicate that the best catalytic performance of the investigated ferrites is the NiCoF-gl sample. It is acceptable because this sample exhibits the relatively highest specific surface area and the lowest particle size, as those parameters are all central factors affecting catalytic efficiency.

More noticeably, the obtained results show that the heat release of AP was increased greatly in the presence of nano-ferrite samples. The heat releases of the AP/ferrite mixtures
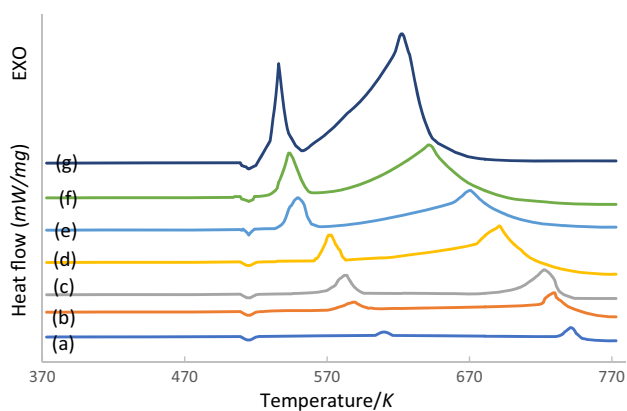
Fig. 6 DSC curves of the AP decomposition in the absence and presence of $Ni_xCo_{1-x}Fe_2O_4$ ($x=0$, 0.05, and 1) ferrite at a 2% mass basis: **a** pure AP, **b** AP+CoF, **c** AP+NiF, **d** AP+NiCoF-cer, **e** AP+NiCoF-gr, **f** AP+NiCoF-mic and **e** AP+NiCoF-gl

were 0.82, 0.89, 0.91, 0.98, 1.04, and 1.23 kJ g^{-1} of AP, for CoF, NiF, NiCoF-cer, NiCoF-gr, NiCoF-micr, and NiCFo-gl, respectively, compared to 0.72 kJ g^{-1} for neat AP.

Kinetic studies

The TGA curves of pure AP and the mixture of the ferrites and AP at a heating rate of 10 K min^{-1} are shown in Fig. 7. All curves show two continuous thermal decomposition steps which will be denoted as the low-temperature decomposition (LT) and high-temperature decomposition (HT). These results agree well with those observed by others [68, 69]. It can be also seen that the existence of ferrites in the decomposition process causes a decrease in the decomposition temperatures of the two steps in the order: NiCoF-gl > NiCoF-mic > NiCoF-gr > NiCoF-cer > NiF > CoF > AP. Thus, the enhancement in the thermal decomposition of AP can be essentially attributed to the catalytic impact of ferrite nanoparticles.

Table 3 Data of the AP decomposition in the absence and presence of 2 mass% $Ni_xCo_{1-x}Fe_2O_4$ ($x=0$, 0.05, and 1) ferrites. PT, LT, and HT represent crystallographic transition endothermic peak temperature, low-temperature decomposition, and high-temperature decomposition (HT), respectively

Sample	PT peak/K	LT peak/K	HT peak/K
Pure AP	518.1	610.1	742.2
AP+CoF	518.2	588.2	730.3
AP+NiF	517.9	583.1	724.2
AP+NiCoF-cer	518.1	572.4	692.1
AP+NiCoF-gr	517.9	548.3	671.2
AP+NiCoF-mic	518.2	542.2	641.3
AP+NiCoF-gl	518.1	533.3	623.1

Kinetics of thermal decomposition using isoconversional methods

The thermal decomposition results showed that the NiCoF-gl sample exhibits the greatest catalytic impact on the thermal decomposition of AP, and therefore we used the isoconversional method to study the kinetic parameters for the catalytic reaction of AP using this sample. The results obtained at heating rates of 5, 10, 15, and 20 K min^{-1} are represented in Fig. 8. By applying Kissinger [50], Ozawa–Flynn–Wall (OFW) [51], Kissinger–Akahira–Sunose (KAS) [52], Starink [53] models as well as the model-free method developed by Friedman [54], (listed in Table 1), the apparent activation energy E_a for thermal decomposition can be determined, without knowing the decomposition mechanism. The data (β, α, T, T_p) taken from the TG curves at fraction conversion $0.1 < \alpha < 0.9$ and different heating rates were employed to acquire the apparent activation energy (E_a) for each decomposition step. This is done by plotting each of $\ln\beta/T_p^2$ versus $1/T_p$, $\ln\beta$ versus $1/T_\alpha$ (or T_p), $\ln\beta/T^2$ versus $1/T$, $\ln\beta/T^{1.92}$ versus $1/T^{1.92}$, $\ln(d\alpha/dt)$ versus $1/T$ and employing the linear regressive of least squares method, Fig. 9, to find the apparent activation energy value (E_a) at different α values. The obtained results are given in Tables 4 and 5, which show that for each one of the calculation methods the calculated activation energy values are slightly changed with the change in the degree of conversion α. Moreover, it is noted that the activation energy values evaluated by Kissinger, KAS, Strain, and Friedman are close to each other and differ slightly from those found by OFW.
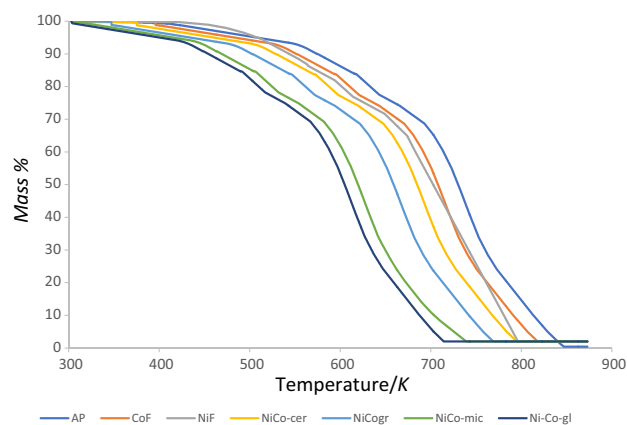

Fig. 7 Thermal decomposition of pure ammonium perchlorate and 2 mass% of the investigated ferrites
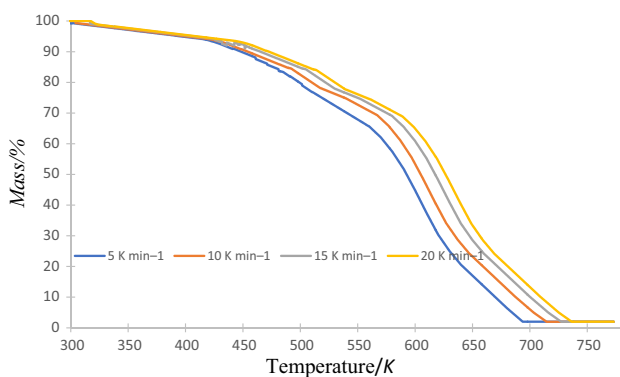
Fig. 8 Thermal decomposition of Ammonium perchlorate with NiCoF-gl sample at different heating rates

Defining the most possible reaction model: $g(a)$ function

To determine the most probable reaction models $g(\alpha)$, the following equation is used

$$\ln g(\alpha) = \left[\ln \frac{AE_a}{R} + \ln \frac{e^{-x}}{x^2} + \ln h(x)\right] - \ln \beta \qquad (14)$$

$h(x)$ is the fourth Senum and Yang approximation formula [55] and $x = E_a/RT$.

From the slope values of plotting $\ln g(\alpha)$ versus $\ln\beta$, $g(\alpha)$ function can be determined, where the slope of the straight line obtained from the linear correlation coefficient R^2 should be equal to unity. From our data, the obtained results listed in Table 6 showed that A_1 and D_1 are the most
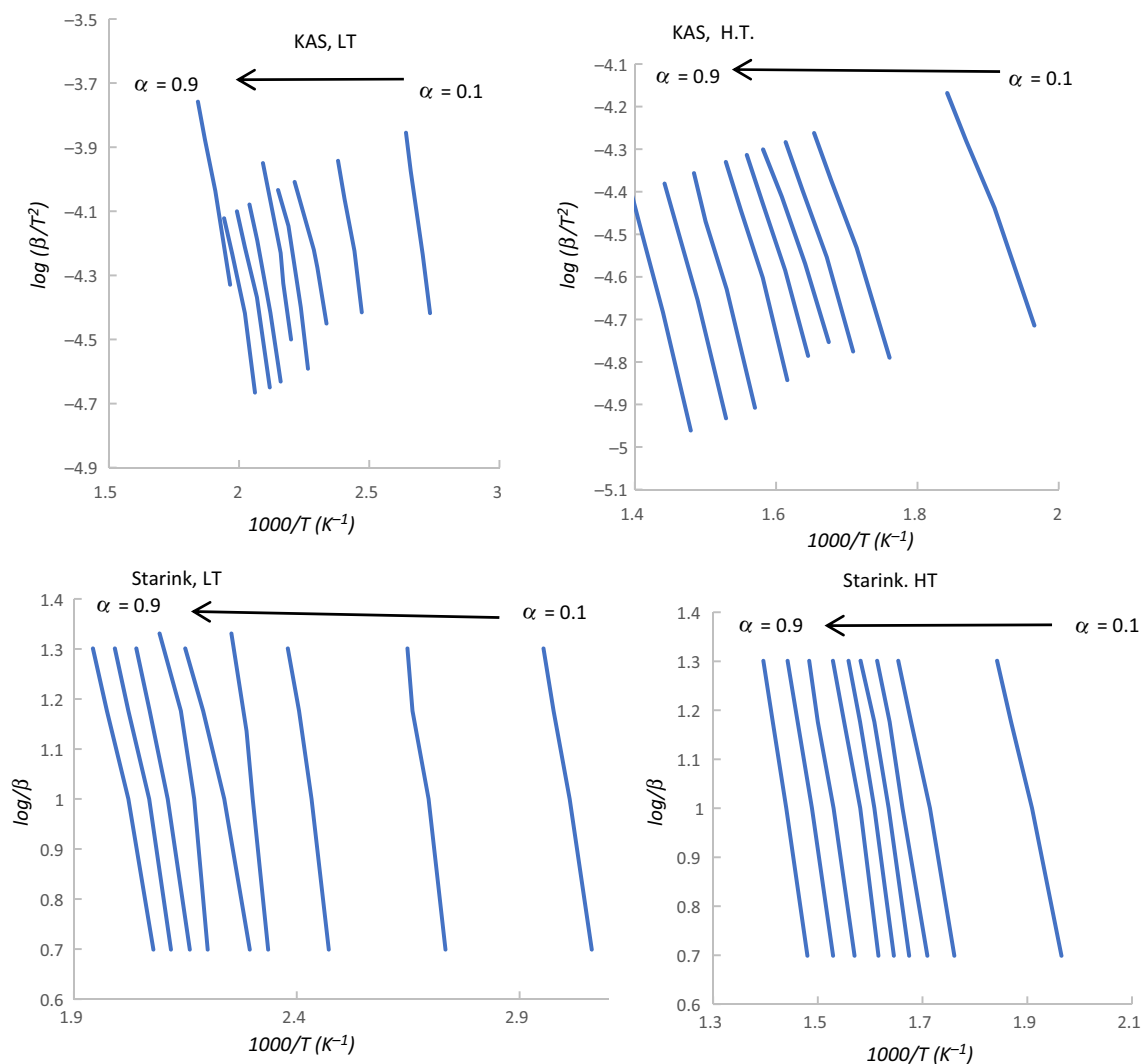

Fig. 9 The plots of the kinetic models A_1 (at lower decomposition temperatures) and D_1 (at higher decomposition temperature) for the catalyzed decomposition of AP using different calculation methods
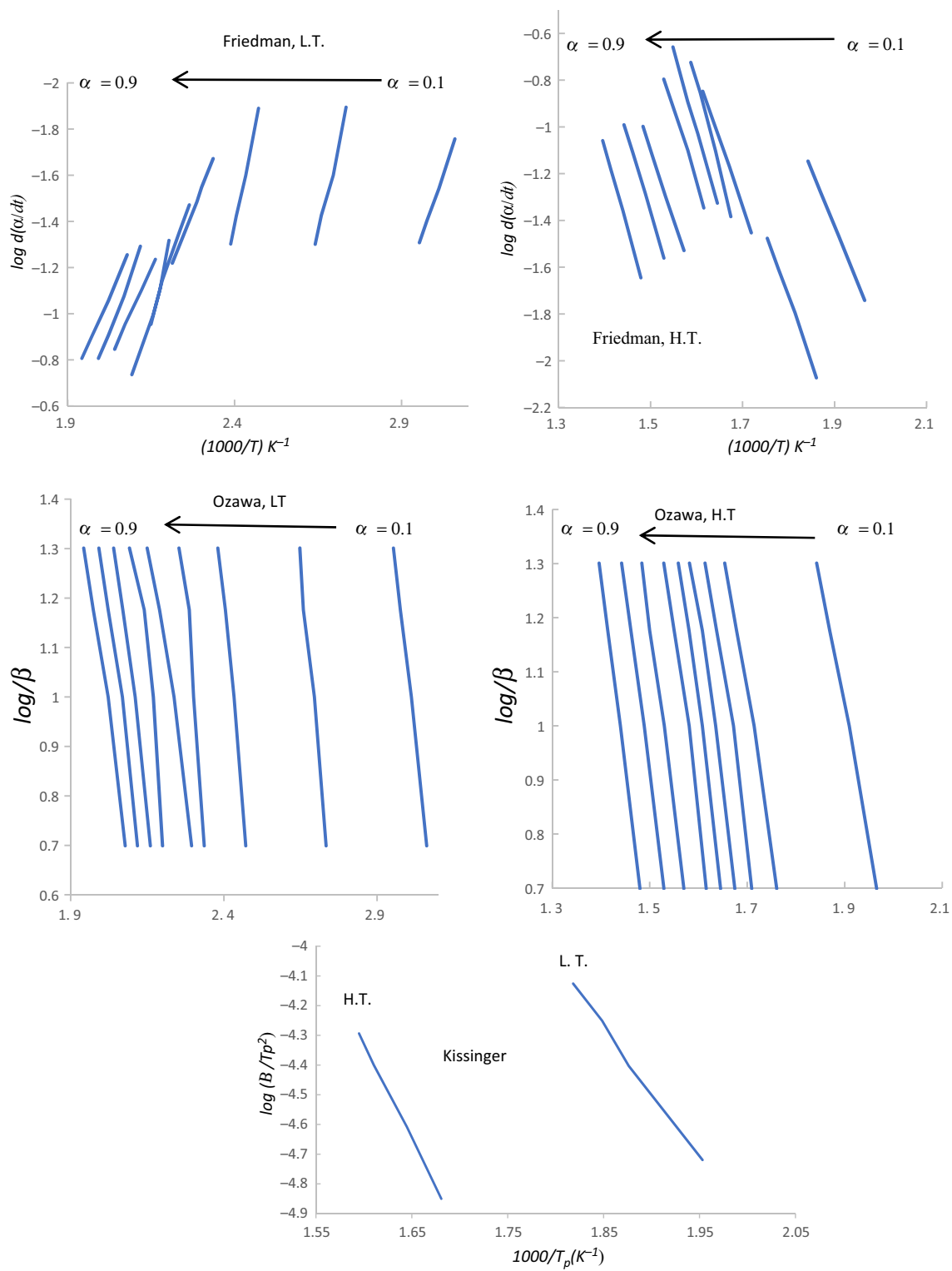
Fig. 9 (continued)

Table 4 Dependence of kinetic parameters on the degree of conversion α at the lower temperatures using OFW, KAS, Friedman, Starink, and Kissinger calculation procedures and using A_1 as a reaction model

Calculation method	Friedman		OFW		KAS		Kissinger*		Starink	
Conversion degree	E_a/kJ mol^{-1}	$A\times10^{-14}$/min^{-1}	E_a/kJ mol^{-1}	$A\times10^{-4}$/min^{-1}	E_a/kJ mol^{-1}	$A\times10^{-4}$/min^{-1}	E_a/kJ mol^{-1}	$A\times10^{-4}$/min^{-1}	E_a/kJ mol^{-1}	$A\times10^{-4}$/min^{-1}
0.1	77.7	1.4	70.3	1.3	82.3	1.5			93.5	1.6
0.2	99.9	1.7	85.6	1.6	91.5	1.6			92.3	1.6
0.3	96.8	1.7	84.2	1.6	96.3	1.7			95.5	1.7
0.4	85.2	1.5	65.1	1.2	78.3	1.4			88.5	1.6
0.5	83.9	1.5	52.9	1.0	93.2	1.7			79.5	1.8
0.6	93.2	1.6	68.9	1.3	95.2	1.7			84.3	1.5
0.7	83.9	1.5	63.8	1.2	84.4	1.6			95.7	1.7
0.8	85.5	1.5	60.2	1.1	82.2	1.6			90.3	1.6
0.9	90.4	1.6	65.0	1.3	84.5	1.6			84.0	1.6
Average	88.3	1.6	70.8	1.3	88.2	1.6	85.7	1.5	89.3	1.7

*E_a-value of Kissinger calculated from DTGA curves

Table 5 Dependence of kinetic parameters on the degree of conversion α at the higher temperatures using OFW, KAS, Friedman, Starink, and Kissinger calculation procedures and using D_1 as a reaction model

Calculation method	Friedman		OFW		KAS		Kissinger*		Starink	
Conversion degree	E_a/kJ mol^{-1}	$A\times10^{-14}$/min^{-1}	E_a/kJ mol^{-1}	$A\times10^{-14}$/min^{-1}	E_a/kJ mol^{-1}	$A\times10^{-14}$/min^{-1}	E_a/kJ mol^{-1}	$A\times10^{-14}$/min^{-1}	E_a/kJ mol^{-1}	$A\times10^{-14}$/min^{-1}
0.1	109.9	6.1	71.7	1.3	101.5	5.9			114.5	6.2
0.2	105.8	6.0	71.6	1.3	105.3	6.1			120.6	6.3
0.3	118.7	6.2	80.6	1.5	105.2	6.0			119.0	6.4
0.4	145.8	6.6	83.4	1.6	113.4	6.2			125.2	6.3
0.5	131.6	6.4	89.0	1.5	117	6.8			133.5	6.5
0.6	118.5	1.6	87.5	1.5	112.0	6.2			131.2	6.5
0.7	114.0	6.2	87.8	1.6	120.5	6.3			131.6	6.5
0.8	125.8	6.3	88.4	1.6	121.3	6.3			122.1	6.3
0.9	135.5	6.4	91.5	1.7	127.2	6.3			122.1	6.3
Average	122.8	6.4	82.4	1.5	113.8	6.4	120	6.4	125.6	6.4

*E_a-value of Kissinger calculated from DTGA curves

probable mechanisms for the catalyzed reaction at LT and HT, respectively.

Establishment of reaction mechanisms

In order to find the kinetic model of thermal decomposition, the Coats–Redfern method [59] was also applied as it involves the degradation mechanisms, as seen in Eq. (12). The kinetic parameters (E_a and $\ln A$) corresponding to each reaction function $g(\alpha)$ are obtained from the plotting of $\ln(g(\alpha)/T^2)$ versus $1/T$. The calculated kinetic parameters (E_a and $\ln A$) for all the kinetic models are recorded in Table 7. Then, they compare with that previously obtained using the four model-free methods. The catalytic thermal decomposition reaction mechanism should be established when the average of the kinetic parameters based on the Coats–Redfern method is the closest to that of model-free methods [70]. The model-fitting results recorded in Table 7 confirm that A_1 and D_1 are the most probable mechanisms for the catalyzed reaction at LT and HT. Both A_1 and D_1 models have good fitting linearity and the highest R^2-values. This result agrees well with those obtained from the model-free methods.

Proposed mechanism of the catalytic effect

The thermal decomposition mechanism of ammonium perchlorate is not so far completely known due to its complex solid–gas multiphase reaction process. However, our results refer to that the decomposition mechanism of AP goes along two paths: an ionic reaction (at lower temperatures) and a radical reaction (at higher temperatures), which agree well with that reported by others [71–77]. The ionic reaction occurring at lower temperatures is attributed to that the AP is a classic dielectric material; thus, at lower temperatures, the probability of the decomposition process via electron transfer is very low. At the LTD, nuclei formation processes occur on the surface of the catalyst which causes the reaction

Table 6 The shape of the most probable mechanism function $g(\alpha)$, slope, and the correlation coefficients of linear regression R^2 for catalyzed thermal decomposition of AP by NiCoF-gl

Temperature range/K	Mechanism	$g(\alpha)$-function	Slope	R^2
420–540	A_1	$-\ln(1-\alpha)$	-1.005986	0.99997
420–540	A_2	$[-\ln(1-\alpha)]^{1/2}$	-1.18339	0.99979
420–540	A_3	$[-\ln(1-\alpha)]^{1/3}$	-1.19211	0.99916
420–540	A_4	$[-\ln(1-\alpha)]^{1/4}$	-1.19222	0.99901
540–710	D_1	α^2	-1.004231	0.99991
540–710	D_2	$\alpha + (1-\alpha)\ln(1-\alpha)$	-1.006251	0.99981

to be controlled by the crystal shape and mobility of the gas phase. Therefore, the nucleation model (A_1) was employed for describing the random nucleation processes as a reaction model in the LTD state. Based on the ionic reaction, it is suggested that the thermal decomposition of ammonium perchlorate initiations through a proton transmission from NH_4^+ to ClO_{4-} (Eq. 15) form some intermediated including NH_3 and $HClO_4$

$$NH_4ClO_4 \leftrightarrow NH_4^+ + ClO_4^- \leftrightarrow NH_3(g) + HClO_4(g) \quad (15)$$
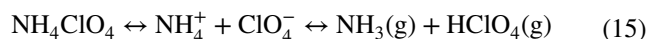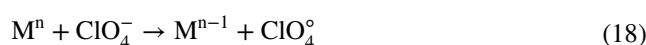
This is followed by several reactions occurring at higher temperatures.

In the HTD state, the D_1 model was found to be the suitable reaction model, because it offers the best fit for the experimental data, as given in Tables 5–7. The adsorption of gaseous products on the AP crystal surfaces is a reaction-limiting factor of AP that delays the diffusion of the gaseous products from the reaction sites. Moreover, the diffusion is also impeded by the crystal lattice of AP, through which gaseous products should pass.

The radical reaction suggests that the decomposition beginning by electron transfer from anion to cation according to the following equation:

$$NH_4^+ + ClO_4^- \rightarrow NH_4 + ClO_4 \quad (16)$$
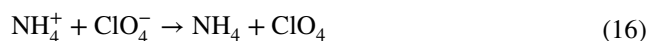
When the ions come nearer to each other, the electrons can be transferred and the ion which is situated in interstices can accept the electron. Accordingly, the catalytic influence of spinel nanoparticles can be attributed to the principle that the ferrite sample is a p-type semiconductor, it exhibits active sites (positive holes on the surface of the catalyst) to receive liberated electron and abstract atomic oxygen from ClO_4^-, according to the following equations:

$$h_{ferrite}^+ + ClO_4^- \rightarrow O_{ferrite} + ClO_3^- \rightarrow \frac{1}{2}O_2 + h_{ferrite}^+ + ClO_3^- \quad (17)$$
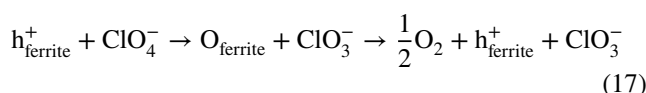
where $h^+_{ferrite}$ symbolizes a positive hole in the valence band of the ferrite and $O_{ferrite}$ is an abstracted oxygen atom from ferrite.

Moreover, the investigated ferrite catalysts have an outermost active not filled with electron d orbitals of Co^{3+} ($3d^6$) and Ni^{2+}($3d^8$), Fe^{3+} ($3d^5$), which can simply accept the liberated electron from ClO_4^- to produce Co^{2+} ($3d^7$), Ni^+($3d^9$, less probable) and Fe^{2+} ($3d^6$) cations, the electron was migrated to the catalyst surface and at the same time contribute in the electron transfer process and speed it by immediate exposure to NH_4^+ and ClO_4^- according to subsequent reactions:

$$M^n + ClO_4^- \rightarrow M^{n-1} + ClO_4^\circ \quad (18)$$

Table 7 Kinetic parameters calculated using Coats–Redfern method for different $g(\alpha)$ function for catalytic thermal decomposition of AP by NiCoF-gel at a heating rate of 10 K min^{-1}

$g(\alpha)$	Lower temperatures			Higher temperatures		
	E_a/kJ mol^{-1}	$A \times 10^{-4}$/min^{-1}	R^2	E_a/kJ mol^{-1}	$A \times 10^{-4}$/min^{-1}	R^2
$F_{1/3}$	76.2	1.5	0.9453	115.7	6.2	0.9783
$F_{3/4}$	73.5	1.4	0.9672	110.6	6.2	0.9634
$F_{3/2}$	71.4	1.4	0.9661	104.9	6.1	0.9543
F_2	69.1	1.3	0.9612	102.4	6.1	0.9632
F_3	65.4	1.2	0.9432	99.6	6.0	0.9543
$P_{3/2}$	85.1	1.9	0.9441	131.3	6.7	0.9666
$P_{1/2}$	61.8	1.2	0.9673	97.5	5.9	0.9554
$P_{1/3}$	63.1	1.2	0.9553	95.5	5.9	0.9432
$P_{1/4}$	66.5	1.3	0.9612	99.8	5.0	0.9341
E_1	59.8	1.1	0.9312	97.2	6.0	0.9531
A_1	87.4	1.6	0.9961	126.6	6.7	0.9653
A_2	84.2	1.8	0.9561	127.7	6.5	0.9634
A_3	77.2	1.5	0.9782	129.2	6.5	0.9543
A_4	75.3	1.4	0.9653	135.9	6.7	0.9555
A_u	71.1	1.3	0.9732	138.1	6.8	0.9623
R_1, F_0, P_1	83.0	1.7	0.9543	142.2	6.9	0.9342
$R_2, F_{1/2}$	84.1	1.8	0.9442	136.5	6.7	0.9633
$R_3, F_{2/3}$	83.9	1.8	0.9543	131.4	6.6	0.9654
D_1	86.1	1.8	0.9342	123.5	6.4	0.9983
D_2	86.9	1.9	0.9432	122.3	6.4	0.9734
D_3	88.6	1.9	0.9621	128.9	6.6	0.9834
D_4	87.5	1.9	0.0534	134.5	6.7	0.9734
D_5	84.2	1.8	0.9331	131.7	6.6	0.9654
D_6	85.8	1.8	0.9432	136.2	6.7	0.9432
D_7	85.5	1.8	0.9532	139.5	6.8	0.9621
D_8	84.9	1.8	0.9342	140.5	6.8	0.9565
G_1	86.5	1.8	0.9433	127.3	6.5	0.9664
G_2	83.1	1.7	0.9312	123.4	6.4	0.9452
G_3	84.1	1.8	0.9379	125.2	6.5	0.9613
G_4	82.2	1.7	0.9453	120.3	6.4	0.9723
G_5	84.6	1.8	0.9389	126.8	6.5	0.9723
G_6	85.7	1.9	0.9452	131.0	6.6	0.9662
G_7	88.8	1.9	0.9634	137.6	6.7	0.9668
G_8	91.4	2.0	0.9543	143.2	6.8	0.9665
B_1	86.6	1.8	0.9634	140.6	6.8	0.9771

$$M^{n-1} + NH_4^+ \rightarrow M^n + NH_4^\circ \tag{19}$$

where M represents the cations present in the spinel.

This means that synergistic effects are possible to happen between the different oxidation states of the cations, which causes the formation of the active sites that aid in progressing the catalytic process. Moreover, because of the large specific surface area of the mesoporous investigated ferrites, the decomposed intermediate produced in the gaseous phase of ammonium perchlorate can be simply adsorbed on the surface of ferrite nanoparticles. Therefore, the addition of ferrite nanoparticles to ammonium perchlorate molecules can spread the contact area of the catalytic reaction,

amplify the active site numbers, which upgrades the thermal decomposition rate of ammonium perchlorate. According to that the NiCoF-gl nanoparticles, which exhibit the highest surface area of all the investigated ferrites, demonstrate the highest catalytic activity than other ferrites.

Thermodynamic parameters

Based on the average activation energy E and the pre-exponential factor A calculated from Eqs. 8 and 9, respectively, through using the most probable $g(\alpha)$ function obtained, the activation thermodynamic parameters, $\Delta S^{\neq}$, $\Delta H^{\neq}$, $\Delta G^{\neq}$, for

the formation of the activated complex were calculated by using Eqs. 20–22.

The change of the entropy is calculated according to the formula:

$$\Delta S^{\neq} = R \ln \frac{Ah}{ek_{B}T_{p}} \qquad (20)$$

where R is the gas constant, e is the Neper number; k_{B} and h are the Boltzmann and Planck constants, respectively, T_{p} is the peak temperature of TG curve and $\Delta S^{\neq}$ is the activation entropy.

The change in enthalpy $\Delta H^{\neq}$ and Gibbs free energy $\Delta G^{\neq}$ for the activated complex formation from the reagents were evaluated using the well-known thermodynamical equations:

$$\Delta H^{\neq} = E - RT_{p} \qquad (21)$$

$$\Delta G^{\neq} = \Delta H^{\neq} - T_{p}\Delta S^{\neq} \qquad (22)$$

The values of $\Delta S^{\neq}$, $\Delta H^{\neq}$, and $\Delta G^{\neq}$ were computed at $T = T_{p}$ (T_{P} is the DTG peak temperature at the corresponding stage), because this temperature symbolizes the highest rate of the decomposition process, and thus, is its important parameter. The results gained are listed in Table 8, in which all the thermodynamic parameters obtained ($\Delta S^{\neq}$, $\Delta H^{\neq}$, and $\Delta G^{\neq}$) are positive, except $\Delta S^{\#}$ for the thermal decomposition at lower temperatures. This indicates that the thermal decomposition of the catalyzed ammonium perchlorate is a fast-nonspontaneous decomposition process and its initiation required the introduction of heat. The $\Delta G^{\neq}$ is a positive value, which approves that the decomposition process will not be started spontaneously. The value of activation entropy ($\Delta S^{\neq}$) is a negative value for the first decomposition step and positive for the second decomposition step. This refers to a decrease in the randomness or disorder of the system when the activation of the molecules occurs at the lower temperatures and an increase in the randomness disorder of the activated molecules at the higher temperatures.

Conclusions

The $Ni_{x}Co_{1-x}Fe_{2}O_{4}[x = 0, 0.5, and 1]$ ferrite nanoparticles were synthesized via the ceramic procedure, whereas the $Ni_{0.5}Co_{0.5}Fe_{2}O_{4}$ was synthesized by green, microwave, and sol–gel method beside the ceramic route. The structure of the synthesized catalysts was studied by XRD, FT-IR spectroscopy, nitrogen adsorption/desorption, SEM, and TEM analyses. The results showed the absence of any impurity in the synthesized nanoparticles with high surface area increases in the order NiCoF-gl > NiCoF-gr > NiCoF-micr > NiCoF-cer > NiF > CoF. The impact of

Table 8 Thermokinetic parameters obtained for the catalyzed thermal decomposition of AP by NiCoF-gl using the most probable mechanism function A_{1} at lower temperatures and D_{1} at higher temperatures

Parameters	Lower temperatures	Higher temperatures
E/kJ mol^{-1}	88.2	122.5
A/min^{-1}	1.6×10^{4}	6.4×10^{14}
$\Delta S^{\#}$/kJ mol^{-1}	-178.4	155.4
$\Delta H^{\#}$/kJ mol^{-1}	86.0	117.4
$\Delta G^{\#}$/kJ mol^{-1}	181.6	116.1

the synthesized catalyst on the thermal decomposition of ammonium perchlorate was investigated by using TGA and DSC techniques. The neat AP was found to decompose in two stages. The prepared ferrites showed a catalytic effect on AP with an efficiency increases with increasing the surface area. The $Ni_{0.5}Co_{0.5}Fe_{2}O_{4}$ sample with the highest surface area of 102.34 m^{2} g^{-1} shifted the high thermal decomposition stage to a lower temperature of about 162 K. The DSC-results showed that the introduction of ferrite NPs has noticeably lowered the thermal decomposition temperature and increased the energy released by the AP/ferrite mixtures to be 0.82, 0.89, 0.91, 0.98, 1.04 and 1.23 kJ g^{-1}, for CoF, NiF, NiCo-cer, NiCo-gr, NiCo-mic, and NiCo-gl, respectively, compared to 0.72 kJ g^{-1} for neat AP. The kinetic parameters of the thermal decomposition steps were determined by using the non-isothermal method for NiCoF-gl (highest catalytic activity and highest surface area). Several calculation methods have been applied and showed that the synthesized catalysts reduced the activation energy value to about 68–79 kJ mol^{-1}, depending on the calculation method and the type of catalyst. The mechanism of thermal decomposition of AP with ferrites was proposed to be A_{1} (random nucleation) for the lower decomposition process and D_{1} (one-dimensional diffusion) for the higher decomposition temperature. The activation energy, pre-exponential factor, and the changes of activated entropy, enthalpy, and Gibbs free energy for the first step catalyzed reaction with NiCoF-gl were evaluated and found to be 82.5 kJ mol^{-1}, 1.6×10^{4} min^{-1}, -178.4 J mol^{-1} K^{-1}, 86.0 kJ mol^{-1} and 181.6 kJ mol^{-1}, respectively; and for the higher decomposition step is 122.5 kJ mol^{-1}, 6.4×10^{14} min^{-1}, 155.4 J mol^{-1} K^{-1}, 117.4, and 116.1 kJ mol^{-1}, respectively. In summary, the results recommend that the as-prepared NiCoF-gl possesses significant catalytic effects on the thermal decomposition of ammonium perchlorate, which can be utilized as a promising additive for increasing the burning rate.

References

1. Campos EA, Pinto DVBS, Oliveira JLS de, Mattos EdaC, Dutra RdeCL. Synthesis, characterization and applications of iron oxide nanoparticles. J Aerosp Technol Manage. 2015;7: 267–76.

2. Yadav N, Srivastava PK, Varma M. Recent advances in catalytic combustion of AP-based composite solid propellants. J Defence Technol. 2020. https://doi.org/10.1016/j.dt.2020.06.007.

3. Rao DCK, Yadav N, Joshi PC. Cu–Co–O nano-catalysts as a burn rate modifier for composite solid propellant. J Defence Technol. 2016;12:297–304.

4. Brewster MQ, Mullen JC. Burning-rate behavior in aluminized wide-distribution AP composite propellants. Combust Explos Shock Waves. 2011;47:200–8.

5. Srivastava P, Dubey R, Kapoor PS, Singh G. Synthesis, characterization and catalytic effect of nimetallic nanocrystals on the thermal decomposition of ammonium perchlorate. Indian J Chem. 2010;49A:1339–44.

6. Sinditskii VP, Egorshev VY. Combustion mechanism and kinetics of thermal decomposition of ammonium chlorate and nitrite: combustion mechanism and kinetics of thermal decomposition. Centr Eur J Energ Mater. 2010;7:61–75.

7. Balzer JE, Siviour CR, Walley SM, Proud WG, Field JE. Behaviour of ammonium perchlorate-based propellants and a polymer-bonded explosive under impact loading. J Proc R Soc A Math Phys Eng Sci. 2004;460:781–806.

8. Chaturvedi S, Dave PN. Solid propellants: AP/HTPB composite propellants. Arab J Chem. 2019;12:2061–8.

9. Xiao X, Peng B, Cai L, Zhang X, Liu S, Wang Y. The high efficient catalytic properties for thermal decomposition of ammonium perchlorate using mesoporous $ZnCo_2O_4$ rods synthesized by oxalate co-precipitation method. J Sci Rep. 2018. https://doi.org/10.1038/s41598-018-26022-2.

10. Han A, Liao J, Ye M, Li Y, Peng X. Preparation of nano-$MnFe_2O_4$ and its catalytic performance of thermal decomposition of Ammonium perchlorate. Chin J Chem Eng. 2011;19(6):1047–51.

11. Li G, Bai W. Synthesis of hierarchical flower-likeCo_3O_4superstructure and its excellent catalytic property for ammonium perchlorate decomposition. J Chem Phys. 2018;506:45–51.

12. Chen L, Li L, Li G. Synthesis of CuO nanorods and their catalytic activity in the thermal decomposition of ammonium perchlorate. J Alloy Compd. 2008;464(1):532–6.

13. Wang Y, Zhu J, Yang X, Lu L, Wang X. Preparation of NiO nanoparticles and their catalytic activity in the thermal decomposition of ammonium perchlorate. Thermochim Acta. 2005;437(1):106–9.

14. Zhang Y, Ma M, Zhang X, Wang B, Liu R. Synthesis, characterization, and catalytic property of nanosized MgO flakes with different shapes. J Alloys Compd. 2014;590:373–9.

15. Zhang Y, Liu X, Nie J, Yu L, Zhong Y, Huang C. Improve the catalytic activity of a-Fe_2O_3 particles in decomposition of ammonium perchlorate by coating amorphous carbon on their surface. J Solid State Chem. 2011;184(2):387–90.

16. Juibari NM, Eslami A. Investigation of catalytic activity of $ZnAl_2O_4$ and $ZnMn_2O_4$ nanoparticles in the thermal decomposition of ammonium perchlorate. J Therm Anal Calorim. 2017;128(1):115–24.

17. Aijun H, Juanjuan L, Mingquan Y, Yan L, Xinhua P. Preparation of nano-$MnFe_2O_4$ and its catalytic performance of thermal decomposition of ammonium perchlorate. Chin J Chem Eng. 2011;19(6):1047–51.

18. Hosseini SG, Abazari R, Gavi A. Pure $CuCr_2O_4$ nanoparticles: synthesis, characterization and their morphological and size effects on the catalytic thermal decomposition of ammonium perchlorate. J Solid State Sci. 2014;37:72–9.

19. Jacobs PWM, Whitehead HM. Decomposition and Combustion of ammonium perchlorate. J Chem Rev. 1969;69:551–90.

20. Cui B, Lin H, Li JB, Li X, Yang J, Tao J. Core-ring structured $NiCo_2O_4$ nanoplatelets: synthesis, characterization, and electrocatalytic applications. J Adv Funct Mater. 2008;18:1440–7.

21. Singh G, Kapoor IPS, Dubey R, Srivastava P. Preparation, characterization and catalytic behavior of $CdFe_2O_4$ and Cd nanocrystals on AP. HTPB and composite solid propellants, Part:79. Thermo-chim Acta. 2015;1–2(511):112–8.

22. Wei SH, Zhang SB. First-principles study of cation distribution in eighteen closed-shell $A^{II}B_2^{III}O_4$ and $A^{IV}B_2^{II}O_4$ spinel oxides. J Phys Rev B. 2001;63(4):045112.

23. Jacobs JP, Maltha A, Reintjes JGH, Drimal J, Ponec V, Brongersma HH. The surface of catalytically active spinels. J Catal. 1994;147(1):294–300.

24. Vozniuk O, Tabanelli T, Tanchoux N, Millet Jean-Marc M, Albonetti S, Di Renzo F, Cavani F. Mixed-oxide catalysts with spinel structure for the valorization of biomass: the chemical-loop reforming of bioethanol. Catalysts. 2018;8:332. https://doi.org/10.3390/catal8080332.

25. Xiao X, Peng B, Cai L, Zhang X, Liu S, Wang Y. The high efficient catalytic properties for thermal decomposition of ammonium perchlorate using mesoporous $ZnCo_2O_4$ rods synthesized by oxalate co-precipitation method. Sci Rep. 2018;8:7571.

26. Modanlou N, Tarighi S. MnC_2O_4 nanoparticles with excellent catalytic activity in thermal decomposition of ammonium perchlorate. J Therm Anal Calorim. 2018;133:1317–26.

27. Chen T, Ping D, Jiang W, Liu J, Hao G, Gao H, Xiao L, Ke X, Zhao F, Xuan C. A facile one-pot solvothermal synthesis of $CoFe_2O_4$/RGO and its excellent catalytic activity on thermal decomposition of ammonium perchlorate. R Soc Chem Adv. 2016;6:83838–47.

28. Alizadeh-Gheshlaghi E, Shaabani B, Khodayari A, Azizian-Kalandaragh Y, Rahimi R. Investigation of the catalytic activity of nano-sized CuO, Co_3O_4 and $CuCo_2O_4$ powders on thermal decomposition of ammonium perchlorate. Powder Technol. 2012;217:330–9.

29. Gheshlaghi EA, Shaabani B, Khodayari A, Kalandaragh YA, Rahimi R. Investigation of the catalytic activity of nano-sized CuO, Co_3O_4 and $CuCo_2O_4$ powders on thermal decomposition of ammonium perchlorate. Powder Technol. 2012;217:330–9.

30. Singh G, Kapoor IPS, Dubey S, Siril PF. Preparation characterization and catalytic activity of transition metal oxide nanocrystals. J Sci Con Proc. 2008;1(7):11–7.

31. Zhang X, Zheng J, Fangb H, Zhang Y, Bai S, He G, Li K. Catalytic decomposition and crack resistance of composite energetic material synthesized by recrystallizing with graphene oxide. Compos A Appl Sci Manuf. 2009;118:90–8.

32. Chaturvedi S, Dave PN, Patel NN. Thermal decomposition of AP/HTPB propellants in presence of Zn nanoalloys. J Appl Nano Sci. 2015;5:93–8.

33. Joshi SS, Paul PR, Krishnamurthy VN. Thermal decomposition of ammonium perchlorate in the presence of nano sized ferric oxide. J Defence Sci. 2008;58(6):721–7.

34. Lucas E, Decker S, Khaleel A, Seitz A, Futlz S, Ponce A, Li W, Carnes C, Klabunde KJ. Nanocrystalline metal oxides as unique chemical reagents/sorbents. Chem A Eur J. 2001;7(12):2505–10.

35. Venkatachalam V, Alsalme A, Alghamdi A, Jayavel R. Hexagonal-like $NiCo_2O_4$ nanostructure based high-performance supercapacitor electrodes. J Ionics. 2017;23:977–84.

36. Velmurugan M, Chen SM. Synthesis and characterization of porous $MnCo_2O_4$ for electrochemical determination of cadmium ions in water samples. J Sci Rep. 2017;7:66. https://doi.org/10.1038/s41598-017-00748-x.

37. Košak A, Makovec D, Drofenik M. The preparation of MnZn-fer-rite nanoparticles in a water/CTAB, 1-butanol/1-hexanol reverse microemulsion. J Phys Status Solidi C. 2004;1(12):3521–4.

38. Khairy M, El-Shaarawy MG, Mousa MA. Characterization and super-capacitive properties of nanocrystalline copper ferrite prepared via green and chemical methods. J Mater Sci Eng . 2021;263:114812.

39. Naghikhani R, Nabiyouni G, Ghanbari D. Simple and green synthesis of CuFe$_2$O$_4$–CuO nanocomposite using some natural extracts: photo-degradation and magnetic study of nanoparticles. J Mater Sci Mater Electron. 2018;29:4689–703.

40. Jalajerdi R, Ghanbari D. Microwave synthesis and magnetic investigation of CuFe$_2$O$_4$ nanoparticles and poly styrene-carbon nanotubes composites. J Nanostruct. 2016;26:278–84.

41. Costa AF, Pimentel PM, Aquino FM, Melo DMA, Melo MAF, Santos IMG. Gelatin synthesis of CuFe$_2$O$_4$ and CuFeCrO$_4$ ceramic pigments. J Mater Lett. 2013;112:58–61.

42. Khawam A, Flanagan DR. Solid-state kinetic models: Basics and mathematical fundamentals. J Phys Chem B. 2006;110:17315–28.

43. Casal MD, Marbán G. Combined kinetic analysis of solid-state reactions: the integral method (ICKA). Int J Chem Kin. 2020. https://doi.org/10.1002/kin.21416.

44. Ninan KN, Krishnan K, Krishnamurthy VN, Ir ley J. Kinetics and mechanism of thermal decomposition of in situ generated calcium carbonate. J Therm Anal. 1991;37:1533–43.

45. Vlaev L, Nedelchev N, Gyurova K, Zagorcheva M. A compara-tive study of non-isothermal kinetics of decomposition of calcium oxalate monohydrate. J Anal Appl Pyrolys. 2008;81:253–62.

46. Atanassov A, Genieva S, Vlaev L. Study on the thermo oxida-tive degradation kinetics of tetrafluoroethylene-ethylene copol-ymer filled with rice husks ash. J Polym Plast Technol Eng. 2010;49:541–54.

47. Khawam A, Flanagan DR. Basics and applications of solid-state kinetics: a pharmaceutical perspective. J Pharm Sci. 2006;95:472–98.

48. Ravi P, Vargeese AA, Tewari SP. Isoconversional kinetic anal-ysis of decomposition of nitropyrazoles. Thermochim Acta. 2012;550:83–9.

49. Vyazovkin S, Sbirrazzuoli N. Isoconversional kinetic analysis of thermally stimulated processes in polymers. Macromol Rapid Commun. 2006;27:1515–32.

50. Kissinger HE. Reaction kinetics in differential thermal analysis. J Anal Chem. 1957;29:1702–6.

51. Ozawa T. Kinetic analysis of derivative curves in thermal analysis. J Them Analy. 1970;2:301–24.

52. Janković B, Smičiklas I. The non-isothermal combustion process of hydrogen peroxide treated animal bones. Kinetic analysis. Ther-mochim Acta. 2011;521:130–8.

53. Dhyani V, Kumar J, Bhaskar T. Thermal decomposition kinetics of sorghum straw via thermogravimetric analysis. J Bioresource Technol. 2017;45:1122–9.

54. Friedman HL. Kinetics of thermal degradation of char-forming plastics from thermogravimetry application to a phenolic plastic. J Polym Sci C Polym Symp. 1964;6:66. https://doi.org/10.1002/polc.5070060121.

55. Senum GI, Yang RT. Rational approximations of the integral of the Arrhenius function. J Therm Anal. 1977;11:445–7.

56. Valanciene E, Miknius L, Pedisius N. The influence of zeolite catalyst on kinetics and thermodynamics of polypropylene waste thermal degradation. J Therm Anal Calorim. 2016;124:341–54.

57. Genieva S, Vlaev L, Atanassov A. Study of the thermooxida-tive degradation kinetics of poly (tetrafluoroethene) using iso-conversional calculation procedure. J Therm Anal Calorim. 2010;99(2):551–61.

58. Vyazovkin S, Burnham AK, Criado JM, Pérez-Maqueda LA, Popescu C, Sbirrazzuoli N. ICTAC kinetics committee recommen-dations for performing kinetic computations on thermal analysis data. Thermochim Acta. 2011;520(1–2):1–19.

59. Ghuge NS, Mandal D. Synthesis of LiDyO2 by solid-state reaction process and study of reaction kinetics by using TG-DTA and XRD techniques. Indian Chem Eng. 2017;59(2):101–16.

60. Khairy M, Bayoumy WA, Selima SS, Mousa MA. Studies on char-acterization, magnetic and electrochemical properties of nano-size pure and mixed ternary transition metal ferrites prepared by the autocombustion method. J Mater Res. 2020. https://doi.org/10.1557/jmr.2020.200.

61. Islam N, Ghosh TB, Chopra KL, Acharya HN. XPS and X-ray diffraction studies of aluminum-doped zinc oxide transparent con-ducting films. J Thin Solid Films. 1996;280:20–5.

62. Srinivasan TT, Srivastava CM, Venkataramani N, Patni MJ. Infra-red absorption in spinel ferrites. Bull Mater Sci. 1984;6:1063–7.

63. Patil RP, Deleka SD, Mane DR, Hankare PP. Synthesis, struc-tural and magnetic properties of different metal ion substituted nanocrystalline zinc ferrite. J Results Phys. 2013;3:129–33.

64. Şabikoğlu I, Paral L, Malina O, Novak P, Kaslik J, Tucek J, Pechousek J, Navarik J, Schneeweiss O. The effect of neodymium substitution on the structural and magnetic properties of nickel ferrite. Prog Nat Sci Mater Int. 2015;25:215–21.

65. Kumar H, Singh JP, Srivastava RC, Negi P, Agrawal HM, Asokan K. FTIR and electrical study of dysprosium doped cobalt ferrite nanoparticles. J Nano Sci. 2014. https://doi.org/10.1155/2014/862415.

66. Pradeep A, Priyadharsini P, Chandrasekaran G. Sol–gel route of synthesis of nanoparticles of MgFe$_2$O$_4$ and XRD, FTIR and VSM study. J Magn Magn Mater. 2008;320(21):2774–9.

67. Compos EA, Fernandes MTC, Kawachi EY, Oliveira JIS, Dutra RCL. Chemical and textural characterization of iron oxide nanoparticles and their effect on the thermal decomposi-tion of ammonium perchlorate. J Propell Explor Pyrotechnol. 2015;40(6):860–6.

68. Juibari MN, Tarighi S. MnCo$_2$O$_4$ nanoparticles with excellent catalytic activity in thermal decomposition of ammonium per-chlorate: green synthesis and kinetic study. J Therm Anal Calorim. 2018;133:1317–26.

69. Shim HM, Lee EA, Kim JK, Kim HS, Koo KK. Formation of tungsten/ammonium perchlorate composites and their reaction kinetics. Cent Eur J Energ Mater. 2015;12:703–22.

70. Ding Y, Ezekoye OA, Lu S, Wang C, Zhou R. Comparative pyrolysis behaviors and reaction mechanisms of hardwood and softwood. J Energy Convers Manag. 2017;132(15):102–9.

71. Joshi SS, Paul PR, Krishnamurthy VN. Thermal decomposition of ammonium perchlorate in the presence of nanosized ferric oxide. J Defence Sci. 2008;58:721–7. https://doi.org/10.14429/dsj.58.1699.

72. Jacobs PMW, Russell-Jones A. On the mechanism of the decom-position of ammonium perchlorate. J Aerosp Res Cent. 2012. https://doi.org/10.2514/3.4085.

73. Essel JT, Nelson AP, Smilowitz LB, Henson BF, Merriman LR, Turnbaugh D, Gray C, Shermer KB. Investigating the effect of chemical ingredient modifications on the slow cook-off violence of ammonium perchlorate solid propellants on the laboratory scale. J Energ Mater. 2020;38:127–41.

74. Wang Y, Song X, Li F. Thermal behavior and decomposition mechanism of ammonium perchlorate and ammonium nitrate in the presence of nanometer triaminoguanidine nitrate. J ACS Omega. 2019;4:214–25.

75. Xiao X, Zhang Z, Cai L, Li Y, Yan Z, Wang Y. The excellent cata-lytic activity for thermal decomposition of ammonium perchlorate

using porous CuCo$_2$O$_4$ synthesized by template-free solution combustion method. J Alloys Compd. 2019;797:548–57.

76. Turmanova S, Genieva S, Vlaev L. Kinetics of nonisothermal degradation of some polymer composites: change of entropy at the formation of the activated complex from the reagents. J Thermodyn. 2011;66:1–10. https://doi.org/10.1155/2011/605712.

77. Vara A, Dave Chaturvedi S. The catalytic activity of transition metal oxide nanoparticles on thermal decomposition of ammonium perchlorate. J Defence Technol. 2019;15:629–35.